Electron temperature profile from optically grey X3-mode of electron cyclotron emission at Wendelstein 7-X using Bayesian analysis

OPEN ACCESS
IOP Publishing
Plasma Physics and Controlled Fusion
Plasma Phys. Control. Fusion **64** (2022) 055016 (13pp)
https://doi.org/10.1088/1361-6587/ac5df3

Electron temperature profile from optically grey X3-mode of electron cyclotron emission at Wendelstein 7-X using Bayesian analysis

Neha Chaudhary*, Matthias Hirsch, Udo Hoefel, Johan W Oosterbeek, Nikolai B Marushchenko, Robert C Wolf and the W7-X Team[1]

Max-Planck Institute for Plasma Physics, Wendelsteinstrasse 1, 17491 Greifswald, Germany

E-mail: neha.chaudhary@ipp.mpg.de

Received 11 December 2021, revised 4 March 2022
Accepted for publication 15 March 2022
Published 12 April 2022

Abstract

The third harmonic extraordinary (X3) mode of electron cyclotron emission is investigated, aiming at its diagnostic capability towards the measurement of electron temperature, T_e, of plasmas with higher densities exceeding the second harmonic extraordinary (X2) mode cutoff. A Bayesian data-analysis approach is adopted through the forward modeling of the X3 emission observations to extract the underlying T_e profile. Bayesian analysis shows that the high field side of the X3 emission spectrum is sufficient to provide the T_e profile. Additionally, for plasma control purposes, a correction factor is provided to track continuous core T_e from the measured radiation temperature of the optically grey X3 emission.

Keywords: electron temperature, electron cyclotron emission, Bayesian statistics, optically grey

(Some figures may appear in colour only in the online journal)

1. Introduction

For fusion relevant plasma parameters, electron cyclotron emission (ECE) from the lower harmonics such as the first harmonic ordinary mode (O1-mode) and second harmonic extraordinary mode (X2-mode) have high absorption coefficients resulting in a high optical depth [1–3]. ECE from these harmonics behave as a black-body emission, and the emission intensities can be directly mapped to the local electron temperature, T_e, of the plasma using Rayleigh-Jeans law. A heterodyne radiometer measures the optically thick X2 emission to provide T_e profile at Wendelstein 7-X (W7-X) [4, 5]. However, for a magnetic field of 2.5 T at the plasma center, the X2 emission has a cutoff at a density, n_e, of $\approx 1.2 \times 10^{20}$ m^{-3} such that it cannot be used as T_e diagnostic for higher density operation of W7-X.

The triple product for stellarators, with confinement time from ISS04 scaling, depends linearly on n_e, and high n_e is required to improve the plasma confinement by increasing the triple product [6, 7]. For a fusion reactor, ECE is also a power loss mechanism, and as an example, for the international fusion project ITER, the estimated ECE power loss at $T_e > 30$ keV and moderate n_e is a significant fraction of heating power [8]. For such scenarios, high n_e is essential to achieve high plasma pressures at reduced T_e to avoid power losses. Moreover, high n_e facilitates divertor detachment [9, 10]. In a burning fusion plasma, high n_e is

[1] See Klinger *et al* 2019 (https://doi.org/10.1088/1741-4326/ab03a7) for the W7-X Team.
* Author to whom any correspondence should be addressed.

advantageous, as it keeps the fast ion population at a low level by reducing the fast ion slowing-down time [11]. Tokamaks have a Greenwald limit on increasing n_e because of the presence of plasma current [12]. The density increase beyond the Greenwald limit typically leads to plasma disruptions terminating the plasma confinement [13]. Because of the absence of toroidal currents, stellarators are not prone to Greenwald density limit, and therefore, it is easier to achieve high densities in a stellarator [14]. Specially, for W7-X, the neoclassical transport optimization [15] favors high n_e. However, there is an upper n_e limit present in stellarators because of the radiation limit set by impurities [16]. Nevertheless, stellarators can use the high-density parameter space for improved plasma confinement. The high n_e operation of W7-X beyond X2 emission cutoff is a motivation for investigating the X3 emission as an extension of ECE parameter space.

The magnetic field gradient along the line of sight of ECE determines the spectral separation of different harmonics. For example, the Joint European Torus (JET) tokamak has a low aspect ratio of ≈3 resulting in steep magnetic field gradient, which leads to the overlapping of the ECE harmonics and complicates the interpretation of the emission spectrum [17]. In contrast, W7-X stellarator has a high aspect ratio of ≈10 which results in a moderate magnetic field gradient along the ECE line of sight (see figure 1) leading to well separated ECE harmonics [18]. Hence, the geometry of W7-X stellarator facilitates the study of the higher ECE harmonics.

At W7-X, the plasma startup and heating is done with the X2-mode of electron cyclotron resonance at 140 GHz using gyrotrons [19]. For fusion reactor relevant conditions, W7-X must operate above the X2 emission cutoff density, which requires additional heating mechanisms. For this purpose, the second harmonic ordinary mode (O2-mode) of electron cyclotron resonance was used for plasma heating as it has a cutoff at a relatively higher n_e of $\approx 2.4 \times 10^{20}$ m^{-3} [20]. Due to the low absorption in the plasma, the O2 heating was done with multiple plasma passes of gyrotron beams. It is essential to control T_e to avoid plasma collapse as the absorption of O2 heating depends on T_e^2. At W7-X, ECE [5], Thomson scattering [21] and x-ray Imaging Crystal Spectrometer can measure T_e. The ECE diagnostic has higher temporal resolution and can provide real-time temperatures which is why this diagnostic is preferred over others for continuous plasma control. Hence, continuous T_e measurement for plasma control during high-density O2 heating is a strong motivation for investigating X3 emission for T_e diagnostic capabilities. The X3 emission measurements have been done previously at different magnetic confinement devices [22–25].

W7-X is also planned to operate at lower magnetic field of 1.7 T for β-limit studies, and for these operations the existing 140 GHz electron cyclotron resonance heating (ECRH) system will be used for plasma heating with X3 polarization instead of X2 [26, 27]. For these conditions, the existing 122–164 GHz radiometer which measures X2-mode at 2.5 T must derive T_e from the X3 emission measurement at 1.7 T. Hence, the lower magnetic field operations of W7-X would benefit from the exploration of the X3 emission.

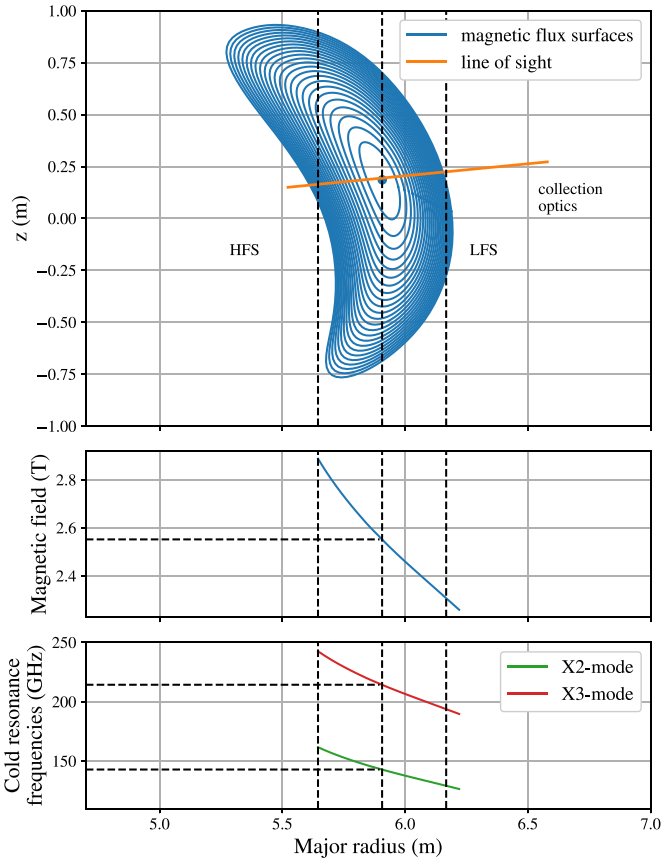

Figure 1. The ECE line of sight through the magnetic flux surfaces is shown and the low field side (LFS) and the high field side (HFS) are marked in the figure. The magnetic field (monotonically decreasing from the inside to the outside of plasma vessel towards observer) and the cold resonance frequencies for second and third harmonics are shown along the line of sight. The ECE antenna (collection optics is marked in the figure) located at the LFS collects the ECE.

A Martin-Puplett interferometer was commissioned to investigate broadband ECE [28–32]. The interferometer was absolutely calibrated with a ceramic black-body source through the hot-cold calibration technique in the spectral range of 100–300 GHz. Interferometer as an ECE diagnostic have been previously used at other magnetic confinement devices [17, 33–36] to provide T_e profile and it will also be used at the international fusion project ITER [37, 38]. The interferometer measures the radiation temperature spectrum, $T_{rad}(f)$, of ECE in a broad frequency range (2–4 harmonics).

The possibility to provide a T_e profile from the ECE depends on precise knowledge of the degree of the re-absorption of the emission in the plasma. For an optically thick plasma, the origin of the emission is spatially localized in the plasma arising from a narrow layer of width ≈1 cm behind the cold resonance. Hence, for the optically thick emission, the T_e profile is extracted through direct inversion of the experimental observed T_{rad}. However, for the scenarios of low optical depth, the emission originates from a broader range of the plasma layers, and includes electrons with different kinetic energies. Hence, an inversion from T_{rad} spectrum to T_e profile

is a non-trivial task. Therefore, a scheme of Bayesian data-analysis is adopted for this work employing forward modeling of the X3 emission to extract T_e from optically thin plasmas. Bayesian analysis and forward modeling of the ECE diagnostic measurements have been done before at different magnetic confinement devices for first and second harmonic ECE [39–42].

This paper presents the Bayesian forward analysis of the interferometer measurements of T_{rad} spectrum around the optically grey X3 emission using radiation transport calculations to infer the T_e profile.

2. Radiation transport calculations for X3 emission

The X3 emission is investigated with calculations of the radiation temperature spectrum, $T_{rad}(f)$ and the optical depth, τ, to identify the plasma parameter regime for direct T_e diagnostic application. Radiation transport calculations were done with the ray-tracing code TRAcing VISualized (TRAVIS) [43], where the ECE branch contains the solver of radiation transport equation along precalculated trajectory back to the receiver. Typically, the ray trajectories are calculated using the cold dielectric tensor (as an option, weakly relativistic approach can be applied), while absorption and emissivity are calculated in fully relativistic approach. Apart from the spectra of radiative temperature, $T_{rad}(f)$, also the radial profile $T_{rad}(\rho)$ is outputted. For the mapping procedure, $f \mapsto \rho$, the spatial location of the emission line is calculated together with its spatial width. Due to this kind of mapping, the profile $T_{rad}(\rho)$ does not have any nonphysical shift (asymmetry with respect to $\rho = 0$) that usually is observed for mapping of frequency to the cold cyclotron resonance location.

In order to cover the case of optically grey plasmas, multi-pass trajectory is calculated. Because of the 3D shape of the plasmas and the reflecting surfaces, the trajectory for each pass is very different. The first reflection is happening at the special tiles installed on the inner wall, and all other ones are happening on the vacuum chamber. The reflection coefficient for all the surfaces is taken in calculations as equal to 1. The effect of depolarization due to reflection is more important. However, the standard way of accounting the scrambling effects [44, 45] is not well applicable for the W7-X. Instead, depolarization due to exit and re-entrance is calculated directly. For the ray which leaves plasmas, polarization is fixed as in point of crossing last closed flux surface (LCFS). When the reflecting surface is met, the polarization is redefined respectively (ideal conductor is supposed), and in the point of re-entrance the wave-field is projected onto the required field for the given wave-mode and from that the wave-mode purity can be obtained.

Since the sight-line (figure 1) for the ECE radiation in the W7-X cannot be strictly perpendicular to the magnetic field and the reflecting surfaces, the points of exit from LCFS and re-entrance are quite different (the distance between of them is approximately 7 cm for the first reflection and about of 23 cm for the second one). As consequence, the wave-mode purity for the first reflection is about 0.8–0.9, depending from the frequency, plasma parameters and magnetic equilibrium. Similarly, for the second reflection the wave-mode purity is about 0.46–0.55. Formally, for accounting the contribution from the reciprocal mode, an additional run can be performed and the sum of both contributions with the corresponding weights gives the expected result.

As a first step the X3 emission was studied with TRAVIS for different T_e and n_e values. To demonstrate the basic effects, the n_e and T_e profiles were chosen to be constant over plasma radius, ρ, and a fixed plasma flux-surface equilibrium was chosen. Additionally, the reflections effects were neglected at the back wall of the plasma vessel for the X3 estimations in this section, as the X3 emission starts to become optically thick for the concerned T_e values.

Figure 2 shows the resulting $T_{rad}(f)$ spectra and optical depth of the X2 and X3 emission. The high density operation of W7-X utilizes O2-ECRH and the absorption of the O2 heating is efficient only above 2 keV. Hence, the chosen T_e values were in the range from 3 to 5 keV and the n_e values were in the range 1.1×10^{20} m^{-3} to 1.3×10^{20} m^{-3}. These plasma parameters reflect the region of interest for the application of the X3 emission as a T_e diagnostic for higher plasma density. For all three T_e values, the X2 emission approximately from 135 to 165 GHz is optically thick with $\tau \geqslant 10$ (for reference $\tau = 3$ already results in 95% absorption), and hence, the T_{rad} is equal to T_e. The X2 emission is only fully present at n_e below 1.1×10^{20} m^{-3} and at a higher n_e, the emission at LFS frequencies, corresponding to lower values of magnetic field along the line of sight (see figure 1), starts to gradually go into cutoff with T_{rad} approaching zero. In contrast, the full X3 emission approximately from 190 to 240 GHz is present at high n_e. For $T_e = 3$ keV, majority of the X3 emission has a value of $\tau \approx 2.5$ except at few frequencies near 200 GHz where $\tau \approx 5$ (see bottom figure 2(b)). At these frequencies, T_{rad} is nearly equal to T_e (see bottom figure 2(a)). For $T_e = 5$ keV, majority of the X3 emission is optically thick with $\tau > 5$ (see top figure 2(b)) and T_{rad} is nearly equal to T_e (see top figure 2(a)). The optical depth for X3 emission from constant plasma profiles is asymmetric (see figure 2(b)). With increasing plasma β and increased diamagnetic downshift in the plasma center, the asymmetry becomes more pronounced as the magnetic field gradient becomes flatter on the LFS and steeper at the HFS.

From the absorption physics of the third harmonic, the optical depth depends strongly on T_e and moderately on n_e [46] and this can be seen in the radiation transport calculations. The simulation results show that X3 emission has a tendency to become optically thick at higher plasma densities and moderate T_e values which can further be explored for the diagnostic purposes. For optically grey emission the radiation temperature is always lower than T_e. Hence, for a direct application of the optically grey X3 emission as T_e diagnostic for plasma control purposes without Bayesian analysis, a correction to T_{rad} is required to derive T_e. For practical purposes, the correction factor C_f is defined by the following equation:

$$C_f = \left(\frac{T_e}{T_{rad}} - 1 \right) \times 100. \tag{1}$$

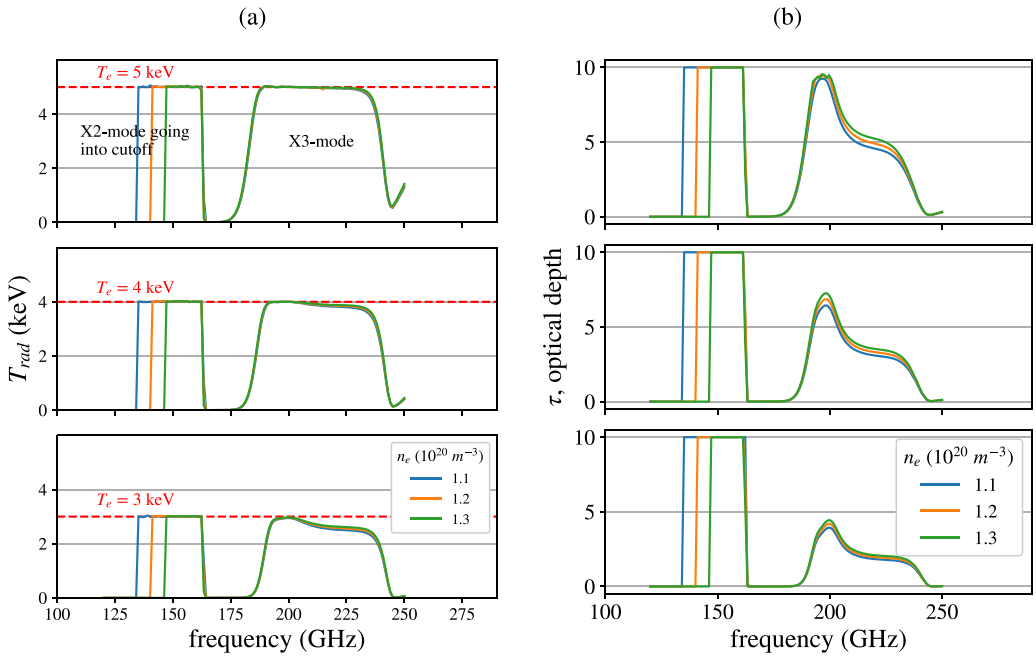

Figure 2. (a) Radiation temperature spectra of ECE covering X2 and X3 emission determined from the radiation transport calculations for three different T_e values of 3 keV (bottom figure), 4 keV (middle figure), 5 keV (top figure). For each value of T_e, n_e is varied from 1.1×10^{20} m^{-3} to 1.3×10^{20} m^{-3} with emission from the plasma center at 140 GHz is more and more shielded by cut-off. The T_e and n_e profiles were chosen to be constant over the whole plasma radius, ρ. (b) The corresponding optical depth (same order for the T_e values). For numerical reasons, the ray tracing is stopped if optical depth, τ, fulfills $e^{-\tau} < 10^{-4}$, and hence, the upper limit of τ is set to $\approx$10.

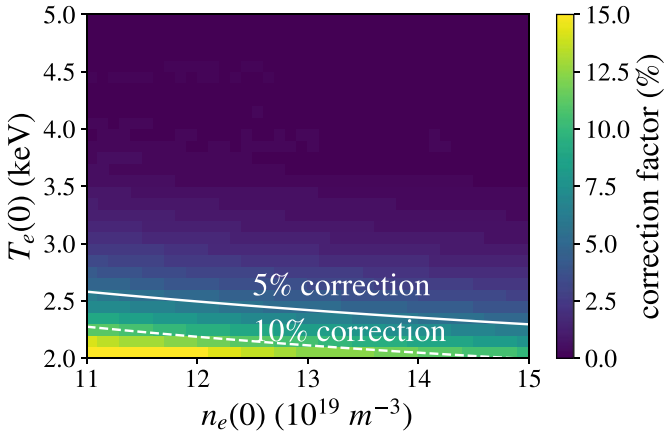

Figure 3. The correction factor scan over T_e and n_e values with constant profile shape over plasma radius. For practical reasons, these calculations correspond to the maximum emission, and hence are not given for a fixed frequency.

Figure 3 shows the correction factor for different T_e and n_e values. The T_e and n_e profile shapes was chosen to be constant over the plasma radius. The correction factor decreases with increased T_e because the re-absorption of X3 emission increases and eventually, the emission becomes optically thick representing the black-body conditions for which the correction factor is negligible. As the optical depth integral has a strong dependence on the T_e profile shape, it was found form TRAVIS calculations that the re-absorption is proportional to the degree of T_e profile broadening.

3. Experimental spectra

A Martin-Puplett interferometer absolutely calibrated with a black-body source was used to measure T_{rad} along the line of sight shown in figure 1 and the details of the diagnostic setup alongside the measurement process are given in [28]. A wire grid beam splitter was used for mode separation at the input to the interferometer. As the emission intensity from the higher ordinary mode (O-mode) harmonics was extremely low, hence only the X-mode emission observations are discussed in this section. Figure 4 shows the plasma profiles and corresponding X-mode emission spectra for three plasma heating scenarios which were available in the first operational phase of W7-X, namely X2-, O2-ECRH and NBI heating. The intensities of ECE harmonics for different plasmas depend on the heating power and fueling. The heating power for these chosen plasmas are as follows: $P_{X2} = 4.5$, $P_{O2} = 6$, and $P_{NBI} = 3.5$ MW. In the case of ECRH, the strong background radiation from non-absorbed 140 GHz microwaves must be suppressed by a notch filter [29]. Hence, the X2 emission (top figure 4(c)) around 130–150 GHz was attenuated because of notch filter, however the X3 and X4 emission were observed. For purely NBI heated plasma (bottom figure 4(c)), the notch filter could be omitted and hence, both X2 and X3 emission were visible simultaneously. There were additional unknown spectral features present near 160 GHz. A possible reason behind these features could be the ECE from toroidally different locations of the stellarator with different magnetic field values reflected to the receiver optics via the vessel walls. The feature around 244 GHz was not from the plasma and it originates from the

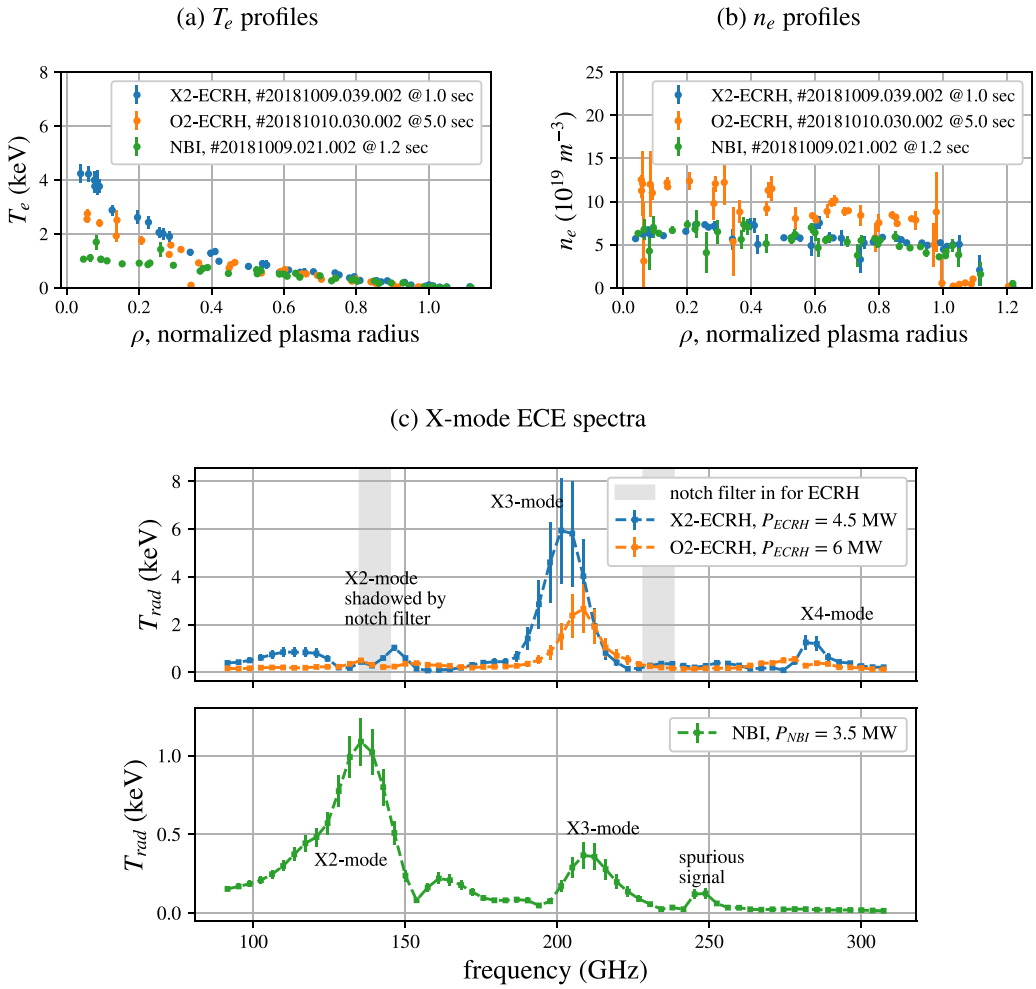

Figure 4. (a) T_e and (b) n_e profiles measured with Thomson scattering diagnostic for three plasma heating scenarios namely X2-, O2-ECRH and neutral beam injection (NBI) heating. The error bars on profiles are only statistical and do not take into account all systematic errors. (c) Broadband extraordinary mode (X-mode) ECE spectra corresponding to the three heating scenarios measured with the interferometer. The error bars on the measurement are from the fitting of the calibration factors using Gaussian processes [28].

radiometer mixer signal, as both the interferometer and the radiometer share the same transmission line. Both ECE diagnostics shared a single wire grid beam splitter [28], which acted as a polarization separator and was used to split the beam between two diagnostics. If X-mode was accessed by the interferometer then radiometer could only access O-mode and vice versa. The second harmonic of the local oscillator of the radiometer mixer leaks into the shared transmission line. The leakage goes from the port of the local oscillator into the input port of the mixer. The local oscillator is of the order of a mW or more, which presents a lot of power compared to the ECE signal in the waveguides and also enters the interferometer. TRAVIS calculations suggests that the X4-mode emission is low at T_e of $\approx$1 keV. As only the O2-ECRH and NBI heated plasmas were capable of achieving high densities, and hence, ECE from these plasmas are discussed in the following sections.

4. Bayesian data-analysis

The Bayesian data-analysis approach is based on the Bayesian probability theory which is a statistical inference. The classical statistical analysis is based on repeating the same experiment under identical conditions to extract the uncertainty of the observation. The drawback of this analysis is that the probability and uncertainty of the experimental observation vary with different numbers of repetitions of the experiment. However, the Bayesian probability is different from the classical probability, as it additionally includes the prior probability knowledge in the random variables or unknown parameters affecting the experiment. Prior probability gets updated with a new data set of measurements or by including additional observations, eventually increasing the knowledge of the experiment and factors affecting it. The increased knowledge on experiment is represented by a posterior probability. The

interpretation of the Bayesian probability for this work is to infer the underlying physics parameters from the observations.

In the context of the experimental observation of $T_{rad}(f)$ affected by assuming only $T_e(\rho)$, the Bayes theorem [47] provides the conditional probability of $T_e(\rho)$ given that the observation of $T_{rad}(f)$ is true:

$$P(T_e(\rho)|T_{rad}(f)) = \frac{P(T_{rad}(f)|T_e(\rho))P(T_e(\rho))}{P(T_{rad}(f))}. \quad (2)$$

The term $P(T_e(\rho))$ is the prior probability representing the knowledge of $T_e(\rho)$ irrespective of the experiment and $P(T_e(\rho)|T_{rad}(f))$ is the posterior probability which represents the updated state of knowledge on the profile with new measurement. The term $P(T_{rad}(f)|T_e(\rho))$ is the likelihood, which links the prior and posterior knowledge on the diagnostic. From Bayes theorem, the posterior probability is the prior probability times the likelihood. The Bayesian inference is characterized by models and parameters. The model is the formulation of how the experimental observation has been obtained from a certain diagnostic and the parameters are the unknown factors or variables affecting this observation. The prior and posterior probabilities are linked by likelihood, which is the forward calculated probability of a certain observation given that the prior knowledge on the parameters is true. The likelihood is determined from the associated model of the diagnostic and its measurement process.

For this work, the forward modeling of the diagnostic is done in the Bayesian Minerva modeling framework [48], which builds on directed acyclic graphical models. The necessary building blocks for the Bayesian data-analysis are the prior probability distribution function which is required to start the forward calculations, the algorithms which can find the position of the maximum *a posteriori* probability (MAP), and the functionality of Markov chain Monte Carlo (MCMC) simulations to sample the posterior distribution.

The diagnostic data-source is an essential part of the forward model as it provides the experimental observations which are compared with the predictions for the Bayesian inference of the free parameters. The main reason to use data-sources is to keep the model as generic as possible. Different diagnostic data-sources are treated as nodes in the graphical models of Minerva framework. This makes it easier to use multiple observations from different diagnostics in the forward model. The Martin-Puplett interferometer data-source provides the raw and analyzed data [28]. The analyzed data consists of absolutely calibrated $T_{rad}(f)$ covering the spectral range of the second and third harmonic ECE and the measurement uncertainties.

In the forward calculations, the $T_{rad}(f)$ is predicted from the radiation transport calculations done with the TRAVIS code and in TRAVIS calculations, the information of the equilibrium is inputted with the VMEC (Variational Moments Equilibrium Code) [49]. The free parameters of the forward model are as follows: T_e profile, n_e profile, X-mode contribution in the detected signal, a scaling parameter for central magnetic field strength and the variance scaling of the observational uncertainties. The predicted T_{rad} is assumed to be a combination of X-mode and O-mode emission in the forward model to take care of any mode mixing effects possibly caused by the leakage of O-mode to X-mode measurements after mode separation. However, more weightage is assigned to X-mode and this weightage is a free parameter in the model and is named as X-mode contribution. A scaling parameter for central magnetic field strength is a free parameter of the model as well. For this work, a uniform distribution priors with an upper and lower limits were chosen for the X-mode contribution factor in the detected signal, for the central magnetic field scaling factor and for the variance scaling factor. The $T_e(\rho)$ and $n_e(\rho)$ were initialized similarly in the model using parameterization [43], which is given by the following equation:

$$T_e(\rho) = a(g - h + (1 + h - g)(1 - \rho^p)^q + h(1 - e^{-\rho^2/w^2})), \quad (3)$$

where a, height at the center, g, height at the edge, h, depth and w, width of hollowness at the center of the profile and two slope parameters, p and q. A uniform distribution function is assigned to each of these parameters, to construct the prior for $T_e(\rho)$ and $n_e(\rho)$.

A graphical model in the Minerva framework represents the Bayesian network of probabilistic nodes and their connections. Figure 5 shows a combined forward model of the Martin-Puplett interferometer and laser interferometer [50] (which measures the line integrated n_e). The addition of laser interferometer observation has the advantage of restricting the line integral of $n_e(\rho)$ profile to a level measured by the experiments. Each box in the graphical model represents a node constructed in Minerva modeling framework. These nodes can be the free parameters (blue boxes), the observations (grey ovals), or the model's physics hypothesis (white boxes). The end of an arrow at a node represents the conditional dependence of that node on other nodes. Nodes that are not connected are conditionally independent of each other.

5. Bayesian inference results

Figure 6 shows the predicted and observed $T_{rad}(f)$ for broadband ECE. It was found that for a single plasma pass of the ECE beam, the prediction of the X2 emission at the HFS frequencies around 135–150 GHz agrees well with the observation. However, the X2 emission at the LFS frequencies (lower than 120 GHz), unknown emission features around 155–180 GHz and moreover, the X3 emission do not agree with the observed data. Hence, as a next step to understand the spectrum better, the reflection effects inside the plasma vessel, were taken into account. Multiple ECE beam passes through the plasma were used for the radiation transport calculations. In addition, the angle of the plasma vessel back-wall tile, at the end of ECE sight-line, was varied in the TRAVIS calculation. These reflection effects, in terms of number of beam passes and back-wall tile angle, cannot be included as a free parameter of the forward model directly. As they were discrete values and the Minerva framework did not allow to have priors

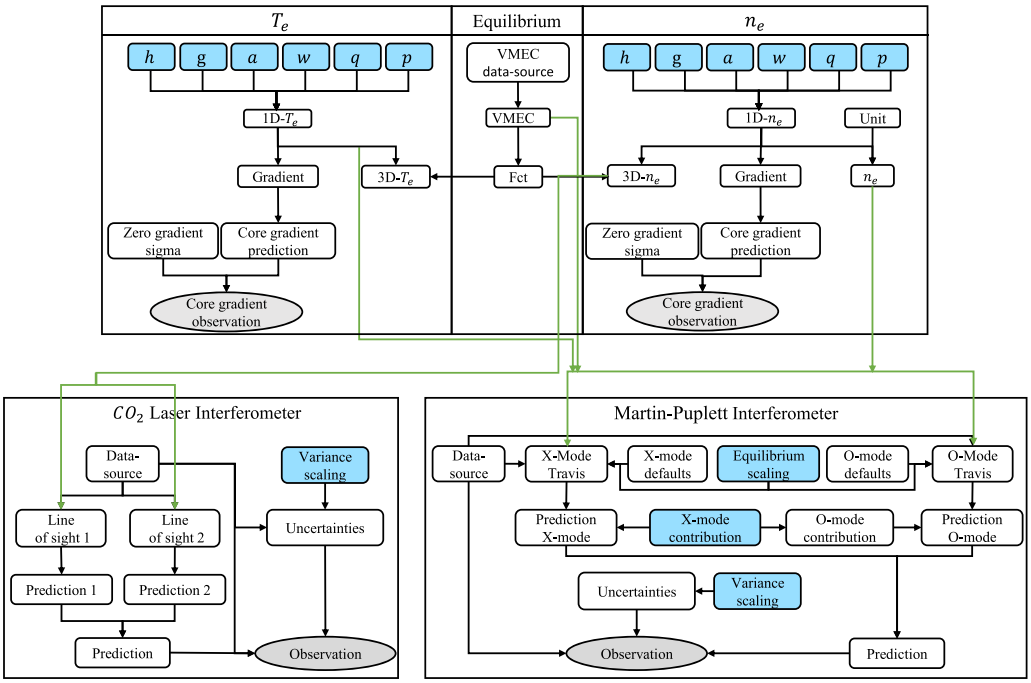

Figure 5. A directed acyclic graph of a combined forward model of the Martin-Puplett interferometer and the laser interferometer diagnostic constructed in the Minerva framework with parametric priors for T_e and n_e profiles. Free parameters of the model are indicated with blue, and the observations with grey color.

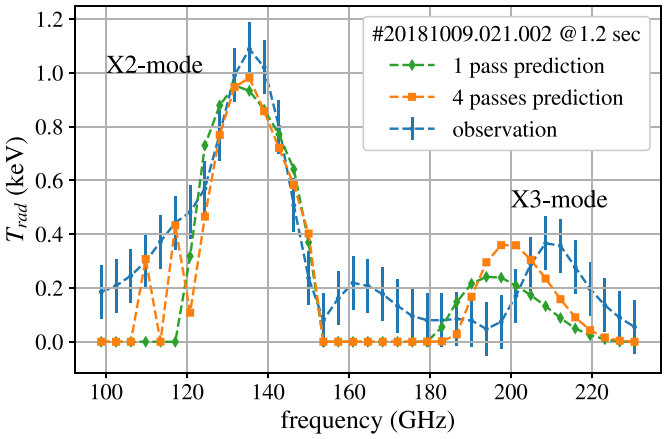

Figure 6. The predicted radiation temperature of ECE from a NBI heated plasma is shown from the forward calculations using parametric priors for the T_e and n_e profiles, for different beam passes through plasma.

with discrete distribution functions. Hence, the beam passes through plasma and tile angle were varied manually, and for each combination of these parameters, the forward calculations were repeated, to find the best prediction. After taking the reflection effects into account, the spectral features that were optically grey are emphasized more as radiation from a larger range of the sight-line is collected such as around 110–120 GHz. For 4 plasma passes, the intensity of the X3 emission increases and shifts to the HFS frequencies, and further increase in the passes did not lead to any improvements in prediction as it saturated. As for multiple reflections of ECE beam in the plasma vessel, the emission is also collected from the neighbouring magnetic field surfaces, and hence, only the optically grey X3 emission shifts to other frequencies and not X2. The maximum T_{rad} of both, the X2 and X3 emission, agree well with the experimentally observed data. However, the frequencies of the X2 and X3 emission simultaneously do not agree with the observational frequencies. While the optically thick X2 emission corresponds to the magnetic field at the single pass sight-line, the optically grey X3 emission is prone of wall reflections. In the stellarator, the magnetic field varies toroidally and poloidally, and the plasma vessel tiles are tilted with respect to the line of sight. The vessel wall reflections of ECE sight-line from these tilted vessel tiles, result in multiple passes of the radiation through plasma in a zigzag path along the changing directions such that ECE from different toroidal and poloidal locations is collected.

Even though multiple beam passes were taken into account and the tile angle was varied for radiation transport calculations, the collected emission could be from sight-lines of the back-wall tiles which pass the plasma at different toroidal or poloidal locations, which were not recovered with these calculations. This could be a possible reason behind the non-optimal prediction of full ECE spectrum from the plasma with rather low T_e. Additionally, the forward calculations were not able to predict the spectral features around 155–180 GHz. This suggests that the physics hypothesis in the forward model was not sufficient for these features and an improved physics model with a more elaborate treatment of reflections [42, 51, 52] is required for spectral prediction in a broadband range. However, a possible explanation of these features could be the relativistically downshifted emission

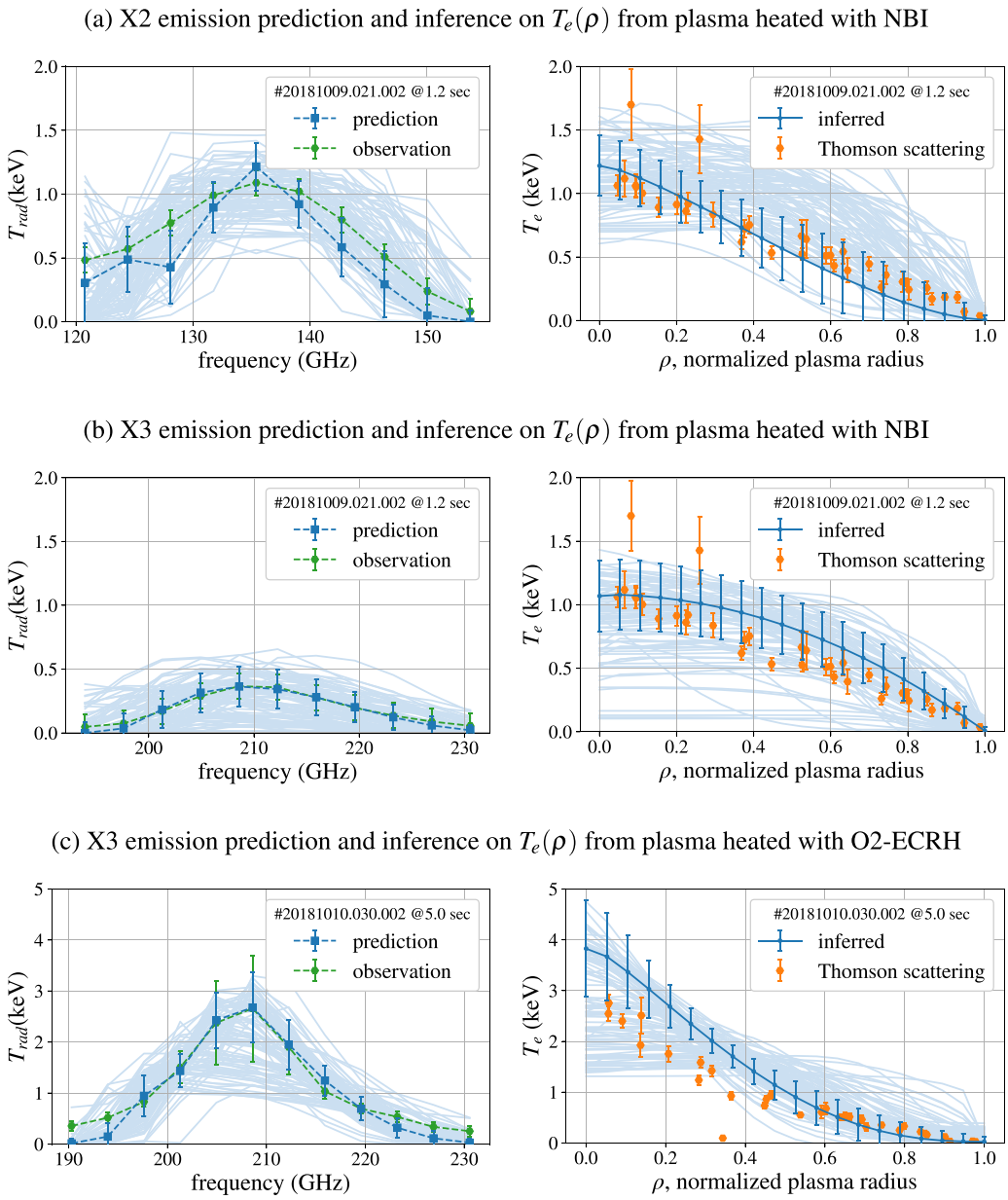

Figure 7. The X2 and X3 emission predicted from the forward calculations, and the corresponding inferred $T_e(\rho)$ profiles are shown. The multiple curves (light blue) are corresponding to the MCMC samples.

from the hot electrons towards the HFS wall, which were reflected and not sufficiently reabsorbed while passing the plasma. The outermost radiometer HFS channels, which are also affected by this feature, show an immediate response with switching of the heating power. It is therefore speculated that it represents the red-shifted emission of hot core electrons which enters the receiver via wall reflections.

The X2 and X3 emission spectra can also be predicted separately to infer the $T_e(\rho)$ and $n_e(\rho)$ profiles. Figure 7 shows the predicted $T_{rad}(f)$ for three measurements, and the inferred T_e profiles from these predictions. The first two measurements were corresponding to the X2 and X3 emission from the same plasma heated with NBI and the third measurement is the X3 emission from an O2 heated plasma. Each spectrum (figure left column) has three curves: the observed $T_{rad}(f)$, the predicted $T_{rad}(f)$ and the MCMC spectra samples covering a wide free parameter space. The error bars on the observation of the T_{rad} spectrum are from the fitting of the calibration factors. The error bars on the prediction of the T_{rad} spectrum are the standard deviation from the MCMC samples. The shift in the predicted center frequency of the X3 emission peak (figure 7(b)) for NBI plasma case compared to the broadband prediction (see figure 6) is the result of the central magnetic field scaling which is a free parameter in the forward model calculations. The T_e profiles (figure right column) represent the profile from prediction of $T_{rad}(f)$. In addition, just for the reference T_e profile from the Thomson scattering measurement [21, 53] is also shown, however it was not used for Bayesian analysis. Note that the errors bars given for the Thomson scattering measurement are purely statistical. Systematic effects were

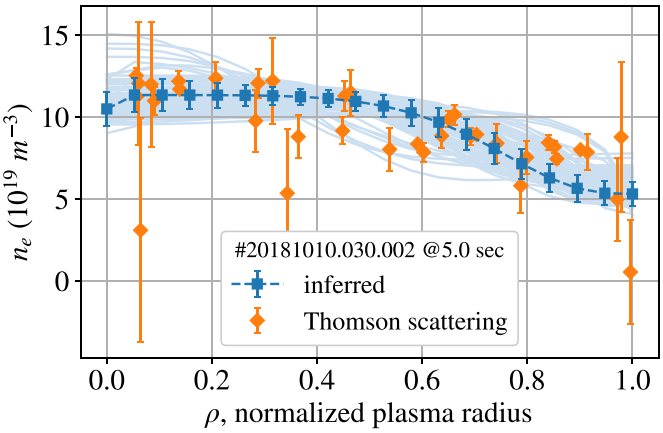

Figure 8. The inferred $n_e(\rho)$ profile is shown from the X3 emission predictions which are discussed in the figure 7(c). The multiple curves (light blue) are corresponding to the MCMC samples.

not taken into account which means that realistic error bars are maybe higher than shown. The inferred T_e profile from the prediction of the X2 emission (see figure 7(a)) agrees well with the Thomson scattering data. For the same plasma, the inferred T_e profile (see figure 7(b)) from the separate prediction of the X3 emission also agrees well with the Thomson scattering data, except few data points near the mid plasma radius, $\rho = 0.5$. For O2 heating, the inferred T_e profile (see figure 7(c)) from predictions of X3 emission also agrees well with the Thomson scattering data near the edge of the plasma at $\rho \geqslant 0.5$. However, near the core of the plasma at $\rho \leqslant 0.5$, the inferred T_e does not agree, and is slightly higher than Thomson scattering data. Possible reasons for the disagreement between two diagnostics could be unaccounted systematic errors of the Thomson scattering measurement [53] or poor calibration of the interferometer at lower frequencies [28]. Moreover, the reason behind disagreement could be that both diagnostics are measuring electrons in different phase space and similar observations have been reported from other magnetic confinement devices as well specially for ECRH plasmas [2].

In a semitransparent or optically grey plasma, the intensity of the ECE depends on the optical depth, thus, also on the plasma density. Hence, the optically grey X3 emission measurements also contain information about n_e profile and it has been used previously to infer n_e [54]. The forward calculation of X3 emission is therefore also capable of inferring the information on the $n_e(\rho)$ hidden in the ECE measurement. Figure 8 shows the inferred $n_e(\rho)$ profile from the X3 emission predictions shown in the figure 7(c). The line integration of the Bayesian inferred $n_e(\rho)$ profile stays within the experimentally observed values as the laser interferometer diagnostic was included in the Bayesian analysis of the X3 emission. It can be observed that the inferred n_e profile from the X3 prediction agrees with the Thomson scattering data.

The inferred T_e and n_e profiles from the predictions discussed in the figures 7 and 8 were used as an input to radiation transport calculations code. The quantities of interest from these calculations are: the optical depth which quantifies the re-absorption of the emission, the velocity of the electrons responsible for the emission and width of the emitting layer. The optical depth of the X2 emission is high, $\tau \geqslant 10$, in most part of the spectrum (see left figure 9(a)). The velocities of the electrons, responsible for this X2 emission, are close to the thermal velocities (see center figure 9(a)). The electron velocity closer to the thermal velocity represents the black-body condition at that emission frequency. Despite the moderate $T_e(\rho) \leqslant 1$ keV in these NBI heated plasmas with high density, the X2 emission remains optically thick. This extends up to the plasma edge at the LFS and the optical depth decreases only moderately towards the HFS edge. The latter is the effect of the HFS plasma boundary which cuts the integral of the optical depth as further out and only a purely absorbing edge plasma exists [55]. The ECE at a given frequency is a distribution of emissions over electron velocities originating from different plasma layers. The effective plasma radius (right figure 9(a)) is the spatial location of the center of mass of the emission distribution at a given frequency. The horizontal error bars on the effective plasma radius represent the width of the emission distribution (or emission layer in the plasma for the specific frequency), while the vertical error bars are from the MCMC samples. The mapping of emission to the effective plasma radius shows that the emission at the LFS frequencies is the downshifted emission from the core electrons and comes from a broader plasma layer (large horizontal error bars). The emission at the HFS frequencies comes from a narrower plasma layer and hence is relatively more localized in the plasma than the emission at the LFS frequencies.

The X3 emission from the purely NBI heated plasma has an optical depth of $\leqslant 0.2$ (left figure 9(b)), which means that the plasma is nearly transparent for this emission. This is also reflected in the electron velocities (center figure 9(b)) as they are higher compared to the X2 emission electron velocities, and also have higher uncertainties. The mapping of the emission to the effective plasma radius (right figure 9(b)) shows that the emission at the LFS frequencies is coming from a broader plasma layer, while the emission at the HFS frequencies is coming from a relatively narrower plasma layer. Hence, the emission at the HFS frequencies is more localized in the plasma than the emission at the LFS frequencies. The reason

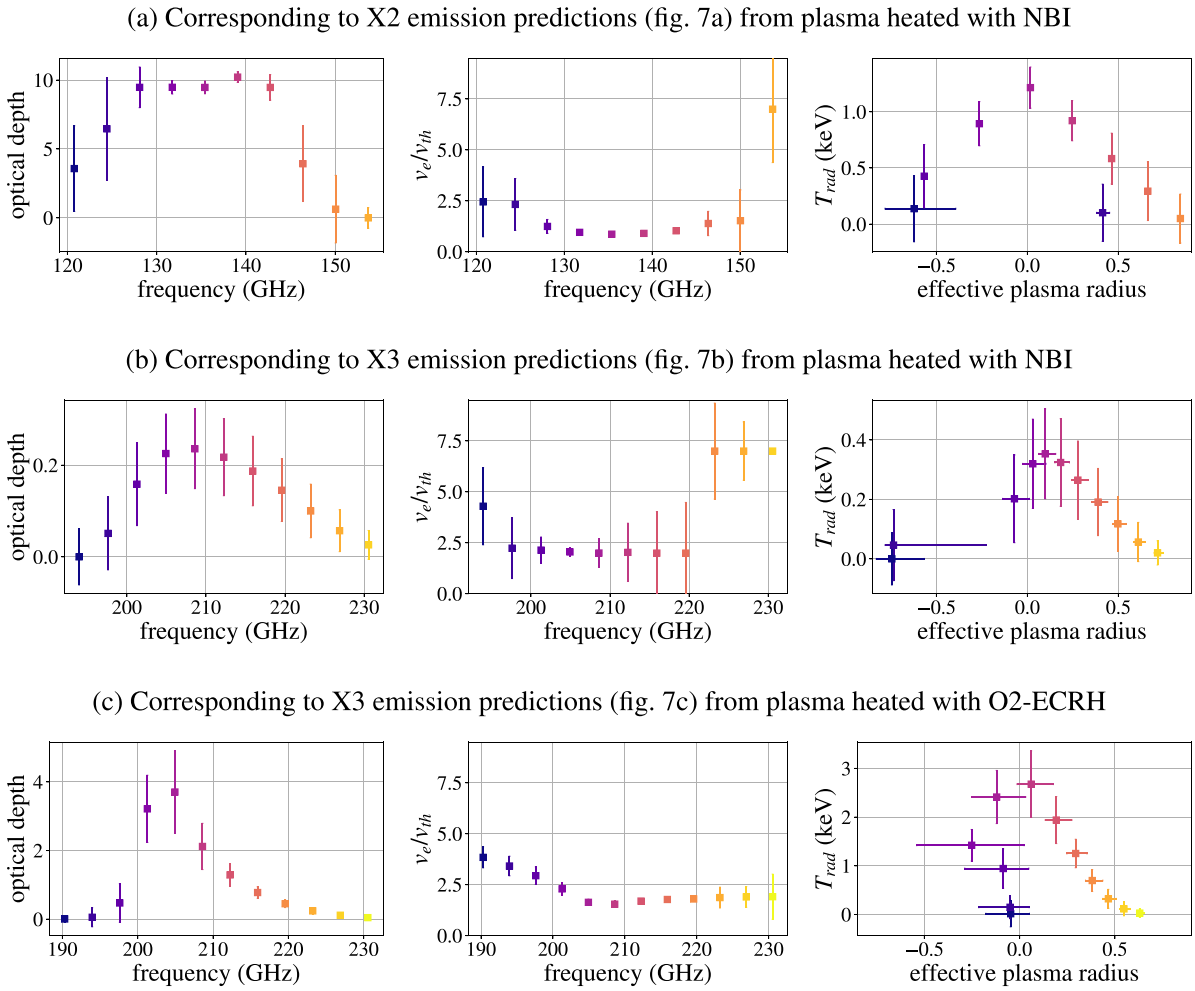

Figure 9. The optical depth of the emission (note the vertical scale for three cases), the velocities of electrons (contributing to emission) normalized to the thermal velocity (v_e/v_{th}), and T_{rad} mapped to the effective plasma radius are shown. The optical depth (left column plots) and electron velocity (middle column plots) at a given frequency and the corresponding effective plasma radius for the emission at that frequency (right column plots) are indicated by the same color. These quantities are calculated with TRAVIS with the input of inferred T_e and n_e profiles discussed in figures 7 and 8. The negative plasma radius represents the plasma location corresponding to the LFS, and the positive plasma radius represents the HFS. The numerical upper limit of this normalized velocity is set to 7, similarly, the upper limit of optical depth is ≈10.

behind this is also the plasma boundary, which cuts the integral of the optical depth.

The X3 emission from the plasma heated with O2-ECRH has slightly higher optical depth ≈3.5 (left figure 9(c)) for part of the spectrum. However, most of the frequencies have a low optical depth leading to optically grey plasma. Only for few frequencies (also where the optical depth is higher ≈3.5) the electron velocity is closer to the thermal velocity (normalized electron velocity is ⩽2) (center figure 9(c)). For the X3 emission at these frequencies, the plasma is optically thick. But for the rest of the frequencies, the plasma is optically grey. From the mapping of the emission to effective plasma radius (right figure 9(c)), the emission at the LFS frequencies is the downshifted emission from the core plasma electrons and is coming from a broader plasma layer. The emission at the HFS frequencies is originating from a narrower plasma layer than emission at the LFS frequencies but it is still less localized than X2 emission. Some degree of localization results as, the emitting layer is limited by the cold resonance on the LFS and by the plasma boundary on the HFS. These results led to the exploration of the inference on T_e profile only from the prediction of the X3 emission only at the HFS frequencies.

Figure 10 shows the prediction of the X3 emission at the HFS frequencies for the measurements from the O2-ECRH plasma (same measurements as shown in left figure 7(c)). In the previous section, for the full X3 emission spectrum prediction, the inferred T_e profile (see right figure 7(c)) near the plasma core did not agree well with Thomson scattering data. However, for the prediction of the same X3 emission spectrum only at the HFS frequencies, already improves the inferred T_e profile (see figure 10(b)) with respect to the Thomson scattering data.

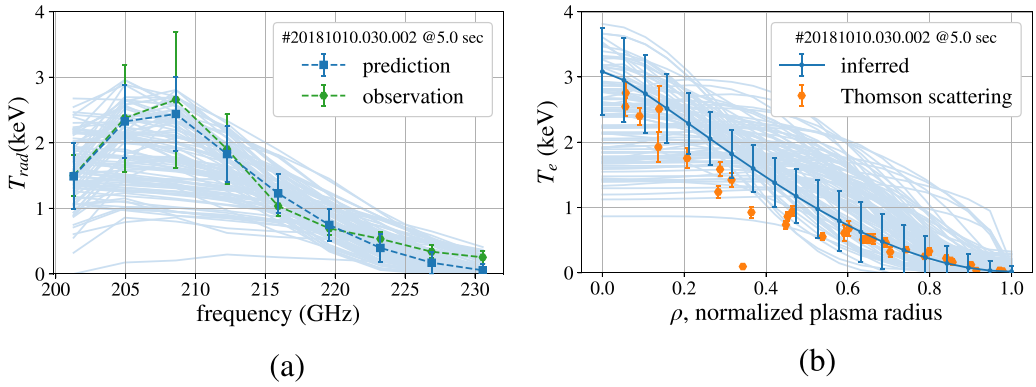

Figure 10. (a) The predicted and observed X3 emission spectra at the HFS frequencies. (b) Corresponding Bayesian inferred $T_e(\rho)$ profile. The multiple curves (light blue) are corresponding to the MCMC samples.

6. Conclusions

The X3 emission has been studied theoretically and experimentally for the geometry of the W7-X stellarator. These studies focus on a higher plasma density application of ECE beyond the X2 emission cutoff at 1.2×10^{20} m^{-3}. To achieve densities above the X2-mode cutoff, plasmas were heated with O2-ECRH. The absorption of O2 heating in plasma depends on T_e^2 and hence, for the control of the O2 heated plasma discharge, T_e should be monitored continuously. For the W7-X specific parameters, it was found that a $T_e \geqslant 2$ keV was required for sufficient absorption of O2 heating power. Hence, the X3 emission was studied using the radiation transport calculations for T_e in a range of 2–5 keV and n_e in a range of 1.1×10^{20} m^{-3}–1.5×10^{20} m^{-3}. At these plasma densities, the X3 emission was found to be optically thick with $\tau \geqslant 3$ for broader T_e profiles having core plasma temperature $\geqslant$3 keV. For the rest of T_e parameter space, the X3 emission was found to be optically grey. Hence, for a direct T_e diagnostic application of optically grey X3 emission, a correction factor to the T_{rad} is provided from the radiation transport calculations. However, the T_e profile shape strongly influences the correction factor and hence, the practical applicability of the correction factor would be improved upon with the experimental knowledge in the next campaign of the W7-X.

During the W7-X operation, the X3 emission was measured with a Martin-Puplett interferometer diagnostic from both O2-ECRH and NBI heated plasmas. For the experimentally available plasma parameters, the measured X3 emission was found to be optically grey at majority of emission frequency range and a direct assignment of a certain frequency to an associated emission layer as in the case of standard ECE diagnostic is not possible. Hence, a classical direct inversion of the measured X3 emission spectrum to a T_e profile is a nontrivial exercise.

A more advanced Bayesian data-analysis approach through the forward modeling of the Martin-Puplett interferometer was adopted to interpret the measured ECE spectrum. Forward calculations of the full X-mode spectrum (100–300 GHz) predicted the measured ECE spectrum well except some unidentified spectral features (around 155–180 GHz). An improved physics model by including better wall reflection modeling is essential for the prediction of the broadband X-mode spectrum. The focus of this particular work is the X3 emission, therefore, two measurements from higher density plasmas heated with NBI and the O2-ECRH were chosen respectively as examples for the Bayesian analysis.

For NBI heated plasma with low $T_e \approx 1.2$ keV, the forward prediction of the X3 emission spectrum generates a T_e profile which agrees well with the Thomson scattering measurements within the inferred uncertainty. The radiation transport calculations done with the generated T_e profile showed that the corresponding X3 emission has a very low optical depth $\tau \leqslant 0.2$. Hence, even for this extreme case of low optical depth, a T_e profile was successfully generated from the measurements of the X3 emission spectrum. Correspondingly, the velocity of electrons responsible for emission is higher than the thermal velocity suggesting that high energy electrons in the tail of the Maxwell–Boltzmann distribution are responsible for the emission. The X3 emission at the LFS frequencies originates from a broader plasma layer suggesting that emission is not localized in the plasma. In contrast, the X3 emission at the HFS frequencies has a narrower emission layer behind cold resonance indicating that the emission at the HFS frequencies is more localized in plasma than emission at the LFS frequencies. The localization of the emission at the HFS frequencies is a result of the plasma boundary and can be understood as the geometrical aspect of localization.

For the O2-ECRH plasma with relatively higher $T_e \approx 2.5$ keV, the generated T_e profile from forward predictions also agrees well with the Thomson scattering measurements within the inferred uncertainty at the plasma edge, however, the generated profile has slightly higher values at the plasma core. The radiation transport calculations done with the generated T_e profile showed that the corresponding X3 emission has relatively higher optical depth $\tau \leqslant 3.5$ approaching nearly black-body conditions. The X3 emission spectrum at the LFS frequencies turns out to be predominantly downshifted emission from the hot core and the broader emission layer suggests that emission is not localized in the plasma. Additionally, the velocity of electrons responsible for the emission at the LFS frequencies is higher than the thermal velocity, hence, the high energy electrons from tail of the Maxwell–Boltzmann distribution are responsible for the emission. In contrast, the X3 emission at the HFS frequencies has relatively narrower

emission layer in the plasma and the emission is more localized because of the geometrical aspect of localization. The velocity of electrons responsible for the emission at the HFS frequencies is relatively closer to thermal velocity, hence, the low energy electrons from the Maxwell–Boltzmann distribution are responsible for the emission suggesting that emission is optically black. From Bayesian analysis results, it can be concluded that the emission at the HFS frequencies is more localized irrespective of optical thickness. Hence, as a next step, only the observations of the X3 emission at the HFS frequencies were predicted and the generated T_e profile agreed well with the Thomson scattering measurements all over the plasma radius.

The paper shows that the X3 emission spectrum is suitable for providing the T_e profiles for the higher density plasmas beyond X2 emission cutoff. Moreover, a measurement of the X3 emission spectrum at the HFS frequencies is preferable and sufficient to provide the T_e profile information.

Data availability statement

The data that support the findings of this study are available upon reasonable request from the authors.

Acknowledgments

This work has been carried out within the framework of the EUROfusion Consortium and has received funding from the Euratom research and training programme 2014–2018 and 2019–2020 under Grant Agreement No. 633053. The views and opinions expressed herein do not necessarily reflect those of the European Commission.

ORCID iDs

Neha Chaudhary https://orcid.org/0000-0001-5075-2487
Robert C Wolf https://orcid.org/0000-0002-2606-5289

References

[1] Costley A, Hastie R, Paul J and Chamberlain J 1974 *Phys. Rev. Lett.* **33** 758
[2] Costley A 2009 *Fusion Sci. Technol.* **55** 1–15
[3] Hartfuß H J and Geist T 2013 *Fusion Plasma Diagnostics with mm-waves: an introduction* (Hoboken, NJ: Wiley)
[4] Klinger T *et al* 2019 *Nucl. Fusion* **59** 112004
[5] Hirsch M *et al* 2019 ECE diagnostic for the initial operation of Wendelstein 7-X *EPJ Web Conf.* vol 203 (EDP Sciences) p 03007
[6] Yamada H *et al* 2005 *Nucl. Fusion* **45** 1684
[7] Dinklage A *et al* 2007 *Nucl. Fusion* **47** 1265
[8] Kukushkin A, Minashin P and Polevoi A 2011 Limit of electron cyclotron radiation in iter long pulse operation *Proc. 38th Conf. on Plasma Physics* vol 35 (*Strasbourg, France*) p 4
[9] Zhang D *et al* 2019 *Phys. Rev. Lett.* **123** 025002
[10] Wolf R *et al* 2019 *Phys. Plasmas* **26** 082504
[11] Wolf R, Beidler C, Dinklage A, Helander P, Laqua H, Schauer F, Pedersen T S and Warmer F 2016 *IEEE Trans. Plasma Sci.* **44** 1466–71
[12] Greenwald M, Terry J, Wolfe S, Ejima S, Bell M, Kaye S and Neilson G 1988 *Nucl. Fusion* **28** 2199
[13] De Vries P *et al* 2011 *Nucl. Fusion* **51** 053018
[14] Helander P *et al* 2012 *Plasma Phys. Control. Fusion* **54** 124009
[15] Beidler C *et al* 2021 *Nature* **596** 221–6
[16] Sudo S, Takeiri Y, Zushi H, Sano F, Itoh K, Kondo K and Iiyoshi A 1990 *Nucl. Fusion* **30** 11
[17] Schmuck S, Fessey J, Boom J, Meneses L, Abreu P, Belonohy E and Lupelli I 2016 *Rev. Sci. Instrum.* **87** 093506
[18] Schmuck S, Hartfuss H J, Hirsch M and Stange T 2009 *Fusion Eng. Des.* **84** 1739–43
[19] Wolf R *et al* 2018 *Plasma Phys. Control. Fusion* **61** 014037
[20] Stange T *et al* 2017 Advanced electron cyclotron heating and current drive experiments on the stellarator Wendelstein 7-X *EPJ Web Conf.* vol 157 (EDP Sciences) p 02008
[21] Pasch E, Beurskens M, Bozhenkov S, Fuchert G, Knauer J and Wolf R (W7-X Team) 2016 *Rev. Sci. Instrum.* **87** 11E729
[22] Austin M, Ellis R, James R and Luce T 1996 *Phys. Plasmas* **3** 3725–31
[23] Bell G and Gandy R 1993 *Nucl. Fusion* **33** 875
[24] Talmadge J, Zushi H, Sudo S, Mutoh T, Sato M, Obiki T, Motojima O, Iiyoshi A and Uo K 1984 *Phys. Rev. Lett.* **52** 33
[25] Sillen R, Piekaar H, Oyevaar T, Gorbunov E, Bagdasarov A and Vasin N 1986 *Nucl. Fusion* **26** 303
[26] Marushchenko N B, Aleynikov P, Beidler C D, Dinklage A, Geiger J, Helander P, Laqua H P, Maassberg H and Turkin Y 2019 Reduced field scenario with X3 heating in W7-X *EPJ Web Conf.* vol 203 (EDP Sciences) p 01006
[27] Nührenberg C 2016 *Nucl. Fusion* **56** 076010
[28] Chaudhary N *et al* 2020 *J. Instrum.* **15** 09024
[29] Chaudhary N, Oosterbeek J W, Hirsch M, Höfel U and Wolf R C 2019 Investigation of optically grey electron cyclotron harmonics in Wendelstein 7-X *EPJ Web Conf.* vol 203 (EDP Sciences) p 03005
[30] Chaudhary N *et al* 2019 Investigation of higher harmonics of electron cyclotron emission in the W7-X stellarator *46th Conf. on Plasma Physics*
[31] Oosterbeek J *et al* 2019 *Fusion Eng. Des.* **146** 959–62
[32] Oosterbeek J W, Chaudhary N, Hirsch M, Höfel U and Wolf R C 2019 Assessment of ech stray radiation levels at the W7-X Michelson interferometer and profile reflectometer *EPJ Web Conf.* vol 203 (EDP Sciences) p 03010
[33] Austin M, Ellis R, Doane J and James R 1997 *Rev. Sci. Instrum.* **68** 480–3
[34] Simonetto A, Sozzi C, Garavaglia S, Fessey J, Nowak S and (Contributors J E) 2011 *Rev. Sci. Instrum.* **82** 113506
[35] Stauffer F, Boyd D, Cutler R and McCarthy M 1985 *Rev. Sci. Instrum.* **56** 925–7
[36] Schmuck S, Fessey J, Gerbaud T, Alper B, Beurskens M, De La Luna E, Sirinelli A and Zerbini M (JET-EFDA Contributors) 2012 *Rev. Sci. Instrum.* **83** 125101
[37] Taylor G *et al* 2015 Status of the design of the ITER ECE diagnostic *EPJ Web Conf.* vol 87 (EDP Sciences) p 03002
[38] Taylor G *et al* 2017 Update on the status of the ITER ECE diagnostic design *EPJ Web Conf.* vol 147 (EDP Sciences) p 02003
[39] Schmuck S, Svensson J, Figini L, Jonsson T, Fessey J, Meneses L and Boom J (JET-EFDA Contributors) 2014 Electron temperature and density inferred from jet ECE diagnostics *Proc. 41st EPS Conf. on Plasma Physics* vol 1 (*Berlin*) p 025
[40] Rathgeber S *et al* 2012 *Plasma Phys. Control. Fusion* **55** 025004

[41] Höfel U 2020 Bayesian analysis of electron cyclotron emission measurements at Wendelstein 7-X *Doctoral Thesis* Technische Universität Berlin, Berlin (available at: http://dx.doi.org/10.14279/depositonce-9621)
[42] Denk S *et al* 2018 *Plasma Phys. Control. Fusion* **60** 105010
[43] Marushchenko N, Turkin Y and Maassberg H 2014 *Comput. Phys. Commun.* **185** 165–76
[44] Costley A, Hastie R, Paul J and Chamberlain J 1974 *Phys. Rev. Lett.* **33** 758–61
[45] Albajar F, Bornatici M and Engelmann F 2005 *Nucl. Fusion* **45** L9
[46] Bornatici M, Cano R, De Barbieri O and Engelmann F 1983 *Nucl. Fusion* **23** 1153
[47] Bayes T 1763 *Phil. Trans. R. Soc.* **53** 370–418
[48] Svensson J and Werner A 2007 Large scale Bayesian data analysis for nuclear fusion experiments 2007 *IEEE Int. Symp. on Intelligent Signal Processing* (IEEE) pp 1–6
[49] Hirshman S P and Whitson J 1983 *Phys. Fluids* **26** 3553–68
[50] Brunner K *et al* 2018 *J. Instrum.* **13** 09002
[51] Rasmussen J *et al* 2019 *Plasma Phys. Control. Fusion* **61** 095002
[52] Farina D, Figini L, Platania P and Sozzi C 2008 Spece: a code for electron cyclotron emission in tokamaks *AIP Conf. Proc.* vol 988 (American Institute of Physics) pp 128–31
[53] Bozhenkov S *et al* 2017 *J. Instrum.* **12** 10004
[54] Clark W 1983 *Plasma Phys.* **25** 1501
[55] Marushchenko N, Dinklage A, Hartfuss H, Hirsch M, Maassberg H and Turkin Y 2006 *Fusion Sci. Technol.* **50** 395–402